

Waxholm Space atlas of the Sprague Dawley rat brain



Eszter A. Papp ^a, Trygve B. Leergaard ^a, Evan Calabrese ^b, G. Allan Johnson ^b, Jan G. Bjaalie ^{a,*}

^a Department of Anatomy, Institute of Basic Medical Sciences, University of Oslo, Oslo, Norway

^b Center for In Vivo Microscopy, Department of Radiology, Duke University Medical Center, Durham, NC, USA

ARTICLE INFO

Article history:

Accepted 1 April 2014

Available online 12 April 2014

Keywords:

Digital brain atlas

Waxholm Space

Sprague Dawley

Rat brain template

Segmentation

Magnetic resonance imaging

Diffusion tensor imaging

Neuroinformatics

ABSTRACT

Three-dimensional digital brain atlases represent an important new generation of neuroinformatics tools for understanding complex brain anatomy, assigning location to experimental data, and planning of experiments. We have acquired a microscopic resolution isotropic MRI and DTI atlasing template for the Sprague Dawley rat brain with 39 μm isotropic voxels for the MRI volume and 78 μm isotropic voxels for the DTI. Building on this template, we have delineated 76 major anatomical structures in the brain. Delineation criteria are provided for each structure. We have applied a spatial reference system based on internal brain landmarks according to the Waxholm Space standard, previously developed for the mouse brain, and furthermore connected this spatial reference system to the widely used stereotaxic coordinate system by identifying cranial sutures and related stereotaxic landmarks in the template using contrast given by the active staining technique applied to the tissue. With the release of the present atlasing template and anatomical delineations, we provide a new tool for spatial orientation analysis of neuroanatomical location, and planning and guidance of experimental procedures in the rat brain. The use of Waxholm Space and related infrastructures will connect the atlas to interoperable resources and services for multi-level data integration and analysis across reference spaces.

© 2014 Elsevier Inc. All rights reserved.

Introduction

Atlases of the brain are commonly used in neuroscience as frameworks for spatial orientation, indexing neuroanatomical location of entities or events being studied, and planning and guidance of experimental procedures. Conventional brain atlases are based on interpretation of histological material stained to reveal cyto-, chemo-, or myeloarchitecture, and consist of series of plates containing drawings of anatomical details as observed from well-defined standard cutting planes. Several such brain atlases are widely used today in both primates and humans (Mai et al., 2007; Martin and Bowden, 2000; Paxinos et al., 1999), and in smaller experimental animals including rodents (Franklin, 1997; Lein et al., 2007; Paxinos and Franklin, 2012; Paxinos and Watson, 1982, 2007; Swanson, 1992, 2004). In rodent atlases, spatial reference is provided by the standard stereotaxic coordinate system based on cranial landmarks aiding precise localization for stereotaxic brain surgery (Paxinos and Watson, 1982).

Recent progress in brain imaging has led to the introduction of a new type of atlas based on volumetric template images of the brain (Aggarwal et al., 2011; Evans et al., 2012; Toga et al., 2006). While limited in resolution compared to microscopy, magnetic resonance imaging (MRI) and diffusion tensor imaging (DTI) volumes acquired with isotropic voxels allow the image to be resliced and viewed in arbitrary

angles without loss of image quality. Further, in these digital image volumes intersecting planes can be studied within the same brain. Atlases are built on top of templates by classifying image voxels into different anatomical labels based on image contrast in the template or other data aligned to the template.

This approach has produced a series of volumetric atlasing templates for the mouse (Aggarwal et al., 2009; Chuang et al., 2011; Johnson et al., 2010; Kovacevic et al., 2005; Ma et al., 2005, 2008) and rat brain (Johnson et al., 2012; Lu et al., 2010; Nie et al., 2013; Rumple et al., 2013; Schwarz et al., 2006; Schweinhardt et al., 2003; Valdes-Hernandez et al., 2011; Veraart et al., 2011). In MRI/DTI datasets, cranial landmarks are not readily recognizable or not present (skull removed), and thus coordinate systems based on in-brain landmarks have been proposed (Kovacevic et al., 2005). In an effort to establish standard spatial reference defined by internal landmarks in the rodent brain, Waxholm Space (WHS, Hawrylycz et al., 2011) was introduced and implemented initially in the mouse brain (Johnson et al., 2010). The highest resolution template published for the rat is from the Wistar strain and contains both MRI and DTI of the same brains (Johnson et al., 2012). These templates are currently aligned to the stereotaxic coordinate system of the Paxinos and Watson atlas.

For the Sprague Dawley strain, equally widely used as the Wistar, the highest resolution MRI/DTI atlas was introduced by Veraart et al. (2011) with 14 structures in selected regions delineated. A more completely delineated whole brain atlas has been lacking. In the present study, we further investigate to which extent high resolution MRI data can be used for detailed brain-wide delineation of a larger number of

* Corresponding author at: Department of Anatomy, Institute of Basic Medical Sciences, University of Oslo, P.O. Box 1105 Blindern, N-0317 Oslo, Norway. Fax: +47 22851278.

E-mail address: j.g.bjaalie@medisin.uio.no (J.G. Bjaalie).

structures. Employing ex vivo MRI data allowing detailed boundary delineation (Jiang and Johnson, 2010; Johnson et al., 2002, 2007, 2010, 2012; Nieman et al., 2006; Veraart et al., 2011), we present a new volumetric atlas for the adult Sprague Dawley brain at a higher resolution than previously reported (MRI at 39 μm and DTI at 78 μm isotropic voxels). The atlas contains 76 anatomical regions along with delineation criteria for multiple types of image contrast. More detailed parcellations are currently ongoing for the hippocampus (L.J. Kjonigsen, T.B. Leergaard, M.P. Witter, and J.G. Bjaalie, in preparation; see also Bjaalie et al., 2013). In this template, we have implemented Waxholm Space in the rat brain for the first time, and documented its definition according to principles compatible with those in the mouse brain. Further, we have connected the atlas to the stereotaxic coordinate system by identifying key cranial landmarks in the template. This creates a platform for interoperability across atlases and coordinate systems in the rat brain.

We envision and encourage this Waxholm Space atlas to be a community resource. The atlas and the underlying template are provided open access, intended for refinement and expansion.

Methods

Diffusion magnetic resonance images were acquired at microscopic resolution from an adult male Sprague Dawley rat at the Duke Center for In Vivo Microscopy. The brain was scanned ex vivo, residing intact in the cranium. T_2 and T_2^* -weighted (gradient echo) anatomical images and diffusion weighted images (DWI, Mukherjee et al., 2008), were acquired, reconstructed, and resampled to a common isotropic resolution of 39 μm . Image contrast in the anatomical MRI and diffusion tensor images was used to delineate 76 brain structures. All original images, the segmentation volume, and a hierarchical catalog of delineated structures are shared through the INCF Software Center (<http://software.incf.org/software/waxholm-space-atlas-of-the-sprague-dawley-rat-brain>).

Animal preparation

All animal procedures and experiments were approved by the Duke University Institutional Animal Care and Use Committee. An adult male Sprague Dawley rat (age 80 days, weight 397.6 g, Charles River, Wilmington, MA, USA) was actively stained with a mixture of formalin and ProHance (Gadoteridol, Bracco Diagnostics, Inc., Princeton, NJ) to increase MRI signal to noise ratio while preserving the tissue (Johnson et al., 2002). The animal was anesthetized by intraperitoneal injection of a mixture of Nembutal (Ovation Pharmaceuticals, Inc., Lake Forest, IL) and butorphanol, and transcardially perfused with 0.9% saline and ProHance (10:1 v:v) for 4 min followed by a flush of ProHance in 10% phosphate buffered formalin (1:10 v:v). The head with the brain in situ within the cranium was removed and stored in buffered formalin for at least 24 h. Tissue was rehydrated by immersion in a 1:200 solution of ProHance/saline for 72 h. The head was trimmed to fit into an acrylic sample holder that fits in the RF coil, and surrounded by fomblin, a per-fluorocarbon that minimizes susceptibility artifacts at the interface.

dMRI image acquisition

Microscopic MRI and DWI data were acquired at the Duke Center for In Vivo Microscopy using a 7 T small animal MRI system (Magnex Scientific, Yarnton, Oxford, UK) equipped with 650 mT/m Resonance Research gradient coils (Resonance Research, Inc., Billerica, MA, USA), and controlled with a General Electric Signa console (GE Medical Systems, Milwaukee, WI). The specimen was imaged in a custom 30 mm diameter \times 50 mm long solenoid RF coil fabricated from a continuous sheet of high-frequency microwave substrate (Roger Corp, Rogers, CT, USA). T_2^* -weighted gradient recalled echo (GRE) anatomic images were acquired using a 3D sequence (TR = 50 ms, TE = 8.3 ms, NEX = 2, $\alpha = 60^\circ$). The acquisition matrix was 1024 \times 512 \times 512 over a

40 \times 20 \times 20 mm field of view (FOV). The Nyquist isotropic spatial resolution was 39 μm . Diffusion tensor datasets were acquired using a spin-echo pulse sequence (TR = 100 ms, TE = 16.2 ms, NEX = 1). Diffusion preparation was accomplished using a modified Stejskal-Tanner diffusion-encoding scheme with a pair of unipolar, half-sine diffusion gradient waveforms (width $\delta = 4$ ms, separation $\Delta = 8.5$ ms, gradient amplitude = 450 mT/m). One b0 image and six high b-value images ($b = 1500 \text{ s/mm}^2$) were acquired with diffusion sensitization along each of six non-collinear diffusion gradient vectors: [1, 1, 0], [0, 1, 1], [1, 0, 1], [1, -1, 0], [0, 1, -1], and [-1, 0, 1]. The acquisition matrix was 512 \times 256 \times 256 over a 40 \times 20 \times 20 mm FOV. The Nyquist isotropic spatial resolution was 78 μm . All images were derived from fully sampled k-space data with no zero-filling. All images had a signal-to-noise-ratio (SNR) of 30 or greater. The long TR relative to T_1 and the long TE relative to T_2 give the b0 image strong T_2 -weighting. We therefore refer to the b0 image as T_2 -weighted below. The SNR for the average isotropic DWI was ~ 120 , and the SNR for the individual DWIs was ~ 62 . The SNR for the T_2^* -weighted gradient echo was estimated ~ 50 . The DWI and anatomical images were acquired in a continuous session and were inherently co-registered.

Image reconstruction and post-processing

After image reconstruction, all MRI volumes were registered to the standard T_2 -weighted b0 image using an Advanced Normalization Tools (<http://www.picsl.upenn.edu/ANTS/>) 9-parameter rigid affine registration to correct for the linear component of eddy current distortions. Diffusion tensors were calculated at each voxel with multivariate linear fitting using the TrackVis and Diffusion toolkit (<http://trackvis.org>). Finally, data were organized into consistent file architecture and archived in NIfTI format (<http://nifti.nimh.nih.gov>) in an onsite Oracle database. Fractional anisotropy (FA) values were computed from the three eigenvalues after tensor decomposition (Le Bihan et al., 2001). All DWI images were resampled with no interpolation to match the voxel size of the higher resolution T_2^* -weighted anatomical dataset using the Matlab (MathWorks, Natick, MA) NIfTI Toolkit. This was necessary for co-viewing the images as overlays during segmentation. An 8-bit binary mask was generated by thresholding the DWI volume using Matlab to hide non-brain structures such as the skull and soft tissue.

Image segmentation

Anatomical regions were delineated using ITK-SNAP software v2.2.0 (Yushkevich et al., 2006; <http://www.itksnap.org>). The MRI data were viewed in ITK-SNAP using the default 16-bit grayscale color map (black to white), where dark areas in the image correspond to low signal intensity and bright areas correspond to high signal intensity. Neuroanatomical boundaries were delineated on basis of image contrast observed in T_2 -weighted, T_2^* -weighted, and diffusion weighted images, including RGB maps of principal eigenvector orientation with fractional anisotropy represented by image intensity (DTI maps). Two standard rat brain atlases were used as initial anatomical reference (Paxinos and Watson, 2007; Swanson, 2004). Additional anatomical criteria (see the Results section) were employed to close anatomical boundaries when these were not unequivocally visible in the MRI or DTI images. The neuroanatomical nomenclature was adopted from the Paxinos and Watson (2007) atlas of the rat brain. The left and right hemispheres of the brain were delineated individually. At one location, a small unilateral magnetic field interference artifact prevented delineation (see also Neuroanatomical delineations in the Results section). The boundary in question was then manually transferred from the other side, taking into consideration a slight left-right tilt of the coronal plane, making structures on the right side of the brain appear 1–2 slices (39–78 μm) towards anterior compared to the left side.

Semi-automatic segmentation was performed in adequate high-contrast regions using the intensity region based SNaP algorithm

implemented in ITK-SNAP, producing a segmentation core for a limited number of structures. Manual segmentation steps were taken iteratively for all delineated regions, performed by a single investigator based on combined observations in the different dMRI maps in coronal, sagittal, and horizontal planes. Our delineation of boundaries was aided by inspection of histological maps provided in the reference atlases (Paxinos and Watson, 2007; Swanson, 2004), as well as by series of histological sections from brains of other Sprague Dawley specimens, cut in coronal, sagittal, and horizontal planes, and stained for myelin (Woelche, 1942) and cytoarchitecture (material from Leergaard et al., 2010; S. Lillehaug, J.G. Bjaalie, and T.B. Leergaard, unpublished results). Thus, changes in T_2 and T_2^* signal intensity were compared to changes in cell densities observed in thionine stained sections from corresponding regions, while changes in DTI color maps were interpreted based on observation of corresponding myelin stained fiber orientations. Structures from the hippocampal and parahippocampal region, delineated in the same template, were taken from a parallel study (L.J. Kjonigsen, T.B. Leergaard, M.P. Witter, and J.G. Bjaalie, in preparation).

Data sharing

Original high resolution anatomical MRI and diffusion weighted image volumes of the presented Waxholm Space template, together with anatomical segmentations and the corresponding label descriptions, are made available through the INCF Software Center (<http://software.incf.org/software/waxholm-space-atlas-of-the-sprague-dawley-rat-brain>) in formats compatible with ITK-SNAP and the Mouse BIRN Atlasing Toolkit (MBAT, Lee et al., 2010), including structure hierarchy in XML (.ilf) format. Volumetric images are provided as standard Neuroimaging Informatics Technology Initiative (NIfTI) files.

Results

Volumetric atlasing template

We present an atlasing template for the Sprague Dawley rat brain consisting of high resolution, contrast enhanced structural (including

T_2 and T_2^* -weighted) and diffusion weighted MR images (Fig. 1). The structural images demonstrate architectural details in both gray and white matter with sufficient contrast and spatial resolution to identify tracts, regions and nuclei. Diffusion weighted maps, FA maps and color maps of principal diffusion orientations in the tissue reveal additional features useful for identifying and completing several anatomical boundaries (Fig. 1). The delineations were primarily based on T_2^* and DTI images, which allow identification of most boundaries as reported below.

Spatial reference system

We have applied Waxholm Space (WHS) on the atlasing template to provide standard spatial reference. WHS has been developed for the rodent brain by the INCF Digital Atlasing Task Force (Hawrylycz et al., 2011; Johnson et al., 2010), and is here implemented for the rat brain for the first time. Waxholm Space employs a continuous three-dimensional Cartesian coordinate system, with its origin set at the decussation of the anterior commissure (Fig. 2). We identified the anterior commissure in the template based on its high contrast in the T_2^* and DTI images, and we located the origin of WHS at the intersection of: a) the mid-sagittal plane, b) a coronal plane passing midway (rostro-caudal) through the decussation of the anterior and posterior part of the anterior commissure, and c) a horizontal plane passing midway through the most dorsal and ventral aspect of the decussation of the anterior commissure (Fig. 2). This definition is compatible with the WHS definition for the mouse brain (Johnson et al., 2010). In the present rat brain template the WHS origin was identified at (NIfTI) coordinates 623 (coronal), 268 (sagittal), and 248 (horizontal).

The WHS coordinate system (Hawrylycz et al., 2011) is defined in a brain oriented in the flat skull position, where the height of cranial landmarks lambda and bregma is at the same horizontal level (Paxinos and Watson, 1982). Our MRI template was acquired approximating this position. Although bony structures are generally invisible in MRI, it was possible to observe the coronal, sagittal, and lambdoid cranial sutures in the T_2^* -weighted images due to diffusion of the contrast agent into the connective tissue. We could thus identify bregma at NIfTI

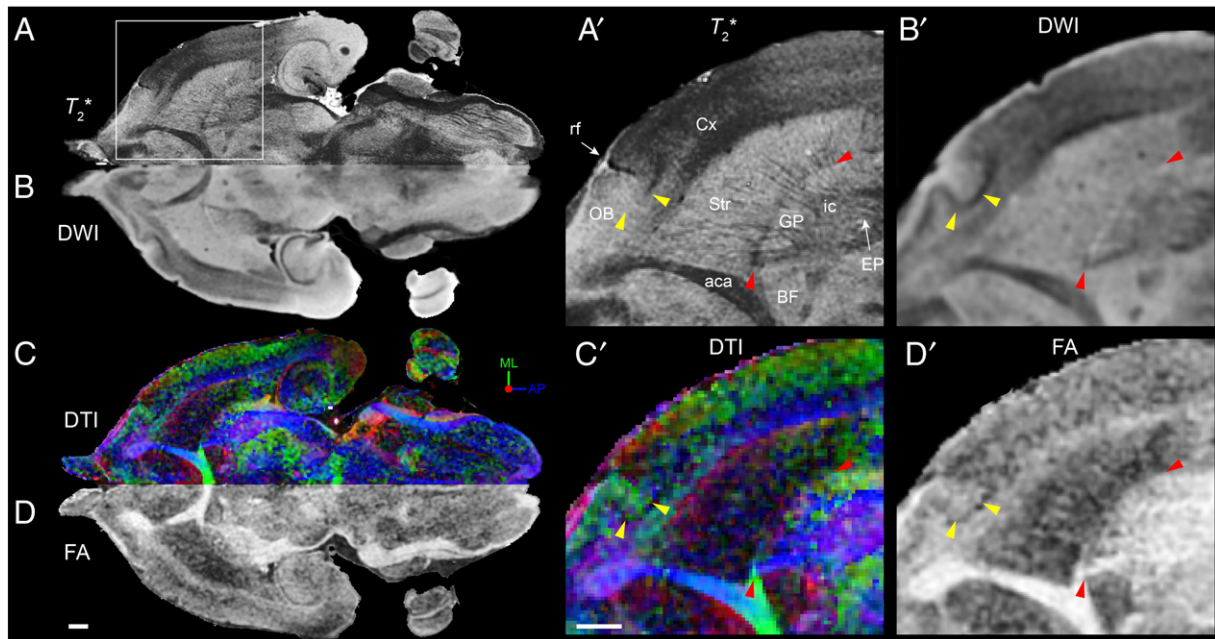


Fig. 1. MRI and DTI contrasts used for anatomical delineations in the atlas: T_2^* -weighted (A, A'); diffusion weighted (DWI; B, B'); diffusion tensor (DTI, C,C'); fractional anisotropy (FA, D,D'). Features observed in the individual images were used in combination to delineate anatomical structures. Frame in A indicates the area enlarged in A'–D'. Yellow arrowheads indicate layer 2 of the piriform cortex, appearing as a continuous band in DWI (B'), but not in the other images. Red arrowheads indicate the boundary between the caudate–putamen complex (striatum) and the globus pallidus, visible as a thin dark line in T_2^* images (A'). Inset in C show the RGB color codes for DTI orientation. aca, anterior part of the anterior commissure; AP, anteroposterior; BF, basal forebrain; Cx, cerebral cortex; EP, entopeduncular nucleus; ic, internal capsule; OB, olfactory bulb; rf, rhinal fissure. Scale bars: 1 mm.

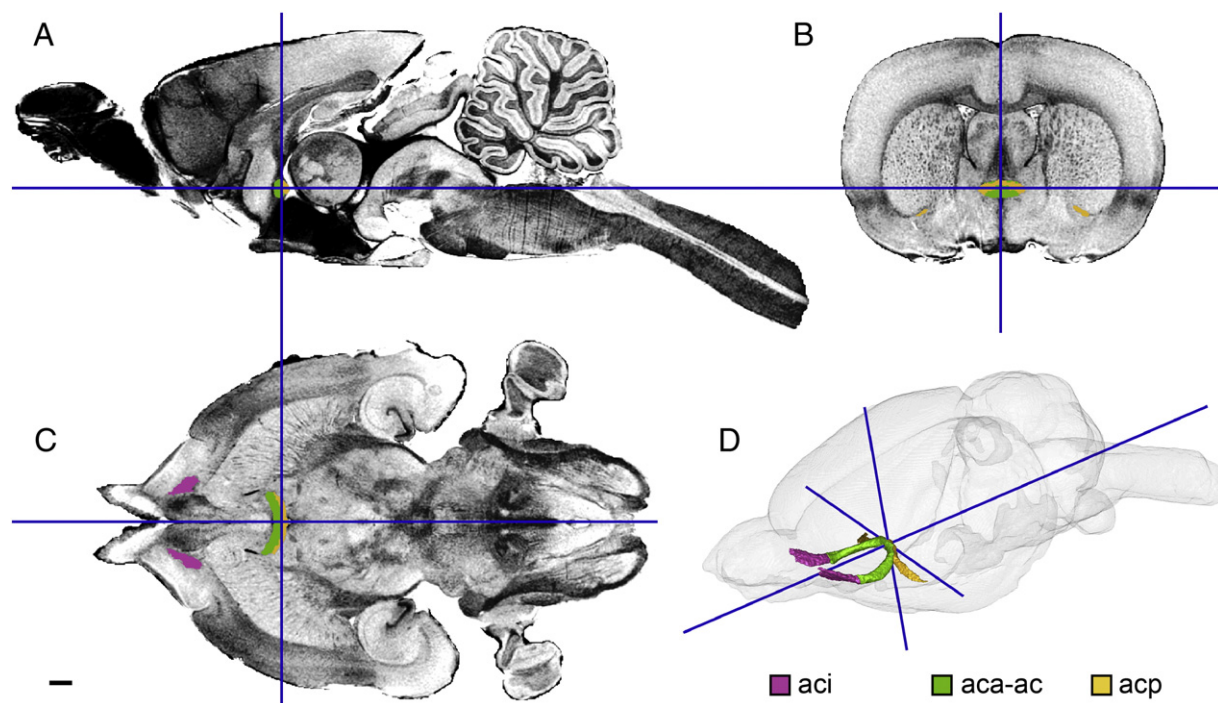


Fig. 2. The Waxholm Space coordinate system. The three axes (blue lines) and the coordinate system origin are identified in relation to the anterior commissure in sagittal (A), coronal (B), and horizontal (C) T_2^* -weighted MRI slices. 3D rendering of the brain surface shows overall position of the origin within the brain (D). For coordinate system definition, see the Results section. aci, intrabulbar part of the anterior commissure; aca, anterior part of the anterior commissure; ac, anterior commissure; acp, posterior part of the anterior commissure. Scale bar: 1 mm.

coordinates 653 coronal; 266 sagittal; and 440 horizontal, and lambda at NIfTI coordinates 442 coronal; 268 sagittal; and 464 horizontal. These coordinates allow the application of the widely used standard skull-based stereotaxic coordinate system (Paxinos and Watson, 1982) to the WHS template. We further also calculated that our spatial template deviates 4° from the flat skull position (Fig. 3B).

Neuroanatomical delineations

For the first release of the atlas, we have delineated 76 anatomical structures (Table 1) on basis of observations in the T_2^* -weighted and diffusion weighted images in combination with relevant information from published atlas resources (Paxinos and Watson, 2007; Swanson, 2004) and literature. The delineations cover the whole brain, including the olfactory bulb and the ventricular system, as well as the spinal cord within 8.62 mm posterior to the skull. White matter bundles form reliable landmarks that are clearly visible in both types of images and are readily distinguished from gray matter regions. Gray matter regions were thus partly defined by surrounding white matter, and partly by more subtle differences in T_2^* and DTI contrast reflecting differences in average cellular density and/or cell diameter. The delineations were manually corrected for a local magnetic field interference artifact (likely caused by bubbles of air or contrast agent trapped at the base of the brain) observed on the right side of the T_2^* image at the level of the subthalamic region. The main criteria used to delineate white and gray matter boundaries, emphasizing observations in T_2^* images and DTI maps, are presented below.

White matter

Corpus callosum and associated subcortical white matter

The corpus callosum, deep cerebral white matter, external capsule, and cingulum constitute a continuous body of subcortical white matter and were delineated as one structure. These structures were differentiated from the cerebral cortex on basis of a distinct difference in FA

value (high signal intensity) and principal diffusion orientation in the DTI maps (Figs. 1, 4, and 5). The cingulum was not separately delineated here, but is readily identified in DTI maps due to its anteroposterior fiber orientation contrasting the mediolaterally oriented callosal fibers (Fig. 5C). The boundary of the external capsule toward the dorsal striatum was clearly seen on basis of gray and white matter contrast visible in the T_2 -weighted and T_2^* -weighted images (Figs. 4D,G). The ventral part of the external capsule forms a thin sheet confining the striatum, and further posterior encompassing the hippocampal formation and the subiculum. The most ventral aspect of this thin sheet is anteriorly best distinguished in DTI (mostly dorsoventral orientation), while the posterior part is best seen in the T_2^* -weighted images (low signal intensity).

Anterior commissure

The anterior commissure was delineated based on its high contrast in both T_2^* and DTI maps (Figs. 1, 2). The structure was divided into an intrabulbar part, located within the olfactory bulb, an anterior part including the decussation, and a posterior part comprising fibers extending ventrolaterally from the anterior commissure between the striatum and the basal forebrain.

Hippocampal white matter

The dorsal hippocampal commissure and its continuation in the alveus form a very thin layer with a thickness close to the voxel size employed (Fig. 5C). In the present version of the atlas, these structures were not separately delineated along the dorsal aspect of the hippocampus, but included as part of the corpus callosum and associated subcortical white matter. The alveus was, however, delineated as a separate structure along the lateral and anterior aspects of the hippocampal formation, distinguished from the medially adjoining fimbria by a slight difference in T_2^* signal intensity. The ventral hippocampal commissure was delineated against the fimbria based on its homogeneous appearance in both DTI (mediolateral orientations, high FA) and T_2^* -weighted images. The horns of the fimbria fill the space between the lateral

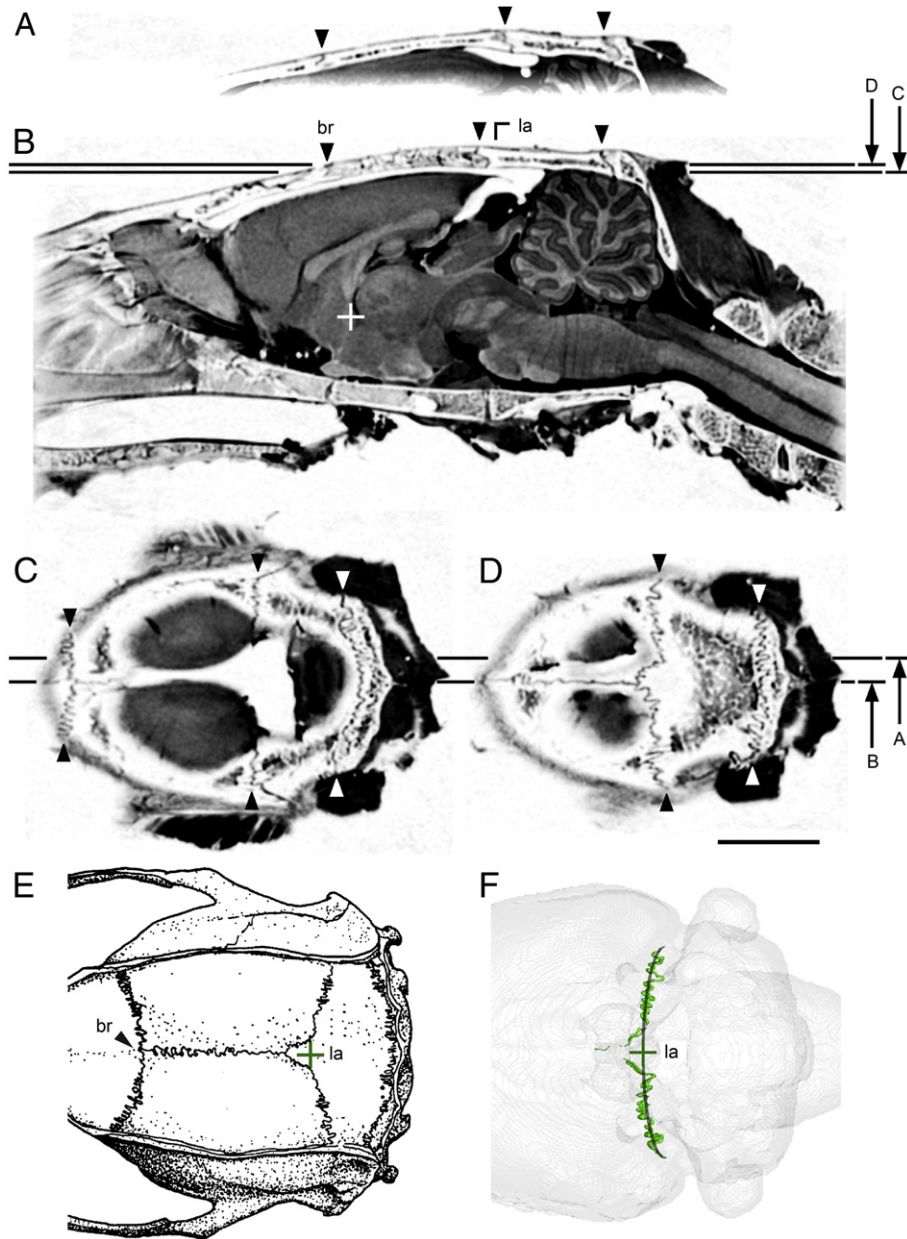


Fig. 3. Stereotaxic skull landmarks identified in the MRI template. A–D show cranial sutures (arrowheads), including the coronal, sagittal and lambdoid sutures, in b0 images with inverted grayscale emphasizing the sutures. The position of the bregma (br) and lambda (la) landmarks is indicated. The WHS origin is marked with a white cross in panel B. E shows bregma and lambda as drawn by Paxinos and Watson (2007). F, 3D reconstruction of the lambdoid suture (meandering green line), matching the drawing shown in E. The lambda landmark is indicated by a green cross at the midpoint of the curve of best fit along the suture (gray line). Scale bar: 5 mm.

ventricles, the hippocampal formation, and the thalamus, as well as the more anteriorly located septal region. The fimbria was delineated against these structures on basis of high FA values and characteristic diffusion orientations (Fig. 5). The boundary between the fimbria and the stria terminalis was identified by the relatively lower T_2^* signal intensity in the fimbria. The fornix was distinguished by its distinct trajectory and its lower T_2^* intensity (Fig. 5A). The interpretation of DTI orientations in these regions was aided by inspection of corresponding myelin stained histological material.

Corticofugal pathways

The corticofugal fiber tracts (Figs. 1, 4–6), including the internal capsule, cerebral peduncle, longitudinal fasciculus of the pons, and the pyramidal tract, were delineated as one continuous structure from the internal capsule to the level of the pyramidal decussation, which was

delineated separately due to its distinct orientation in the brain stem highlighted in DTI maps. The internal capsule was identified by low T_2^* signal intensity in the region located between the striatum and globus pallidus laterally, and the thalamus medially (Figs. 4A,D,G). Dispersed fiber bundles penetrating the striatum were excluded from our delineations. The ventral extent of the internal capsule was delineated using DTI (slightly oblique dorsoventral fiber orientations). DTI maps were also used to delineate the anterior internal capsule against the striatum. Otherwise, the descending fiber tracts were identified on the basis of low T_2^* values, high FA values and the distinct axial diffusion orientations in these tracts. At several levels in the brain stem, the descending pyramidal tract was impossible to differentiate from the adjacent medial lemniscus. Here the dorsal boundary of the pyramidal tract was extrapolated to the expected geometrical shape and position relative to the brain surface and to the midline of the brain.

Table 1

Alphabetical list of white and gray matter structures included in the atlas.

White matter
Alveus of the hippocampus
Anterior commissure, anterior part
Anterior commissure, intrabulbar part
Anterior commissure, posterior part
Ascending fibers of the facial nerve
Brachium of the superior colliculus
Commissural stria terminalis
Commissure of the inferior colliculus
Commissure of the superior colliculus
Corpus callosum and associated subcortical white matter
Corticofugal pathways
Facial nerve
Fasciculus retroflexus
Fimbria of the hippocampus
Fornix
Genu of the facial nerve
Habenular commissure
Inferior cerebellar peduncle
Mammillothalamic tract
Medial lemniscus
Medial lemniscus decussation
Middle cerebellar peduncle
Optic nerve
Optic tract and optic chiasm
Posterior commissure
Pyramidal decussation
Spinal trigeminal tract
Stria medullaris of the thalamus
Stria terminalis
Supraoptic decussation
Transverse fibers of the pons
Ventral hippocampal commissure
Gray matter
Basal forebrain region
Bed nucleus of the stria terminalis
Brain stem
Caudal entorhinal field
Cingulate cortex, area 2
Deeper cerebellum
Deeper layers of the superior colliculus
Dorsal-intermediate entorhinal area
Dorsal-lateral entorhinal area
Entopeduncular nucleus
Frontal association cortex
Globus pallidus
Glomerular layer of the accessory olfactory bulb
Glomerular layer of the olfactory bulb
Hippocampal formation
Hypothalamic region
Inferior colliculus
Inferior olive
Interpeduncular nucleus
Medial entorhinal field
Molecular cell layer of the cerebellum
Neocortex
Nucleus of the stria medullaris
Olfactory bulb
Periaqueductal gray
Perirhinal cortex
Periventricular gray
Pineal gland
Pontine nuclei
Postrhinal cortex
Pretectal region
Septal region
Spinal trigeminal nucleus
Striatum
Subiculum
Substantia nigra
Subthalamic nucleus
Superficial gray layer of the superior colliculus
Thalamus
Ventral-intermediate entorhinal area

Table 1 (continued)

Other structures
Central canal
Spinal cord
Ventricular system

Medial lemniscus

The medial lemniscus was clearly visible with low signal intensity in the T_2^* weighted images from the level of the substantia nigra through the tegmentum to its entry into the thalamus (Fig. 5). At other levels of the brain stem it was hard to distinguish and thus not delineated in the present version of the atlas. The decussation of the medial lemniscus, however, was delineated by its dorsoventral fiber orientation, and separated from the pyramidal decussation by its lower FA values and slightly lower T_2^* signal intensity.

Thalamic tracts

Several distinct white matter tracts associated with the thalamus were clearly visible and delineated on basis of T_2^* -weighted images and DTI maps (Fig. 5; see also Figs. 6F–H). The following tracts were delineated and subsequently used to aid the delineation of the thalamic gray matter: 1) the mammillothalamic tract, 2) the fasciculus retroflexus (of Meynert), providing a prominent white matter landmark at the diencephalic–mesencephalic boundary, 3) the stria medullaris of the thalamus, 4) the habenular commissure, 5) the arc of the stria terminalis (Gloor, 1955; Morgan et al., 2005), and 6) the commissural stria terminalis. At the levels where the stria terminalis adjoins the bed nucleus of the stria terminalis, the two structures were distinguished based on the FA maps. The posterior part of the stria terminalis is intercalated between the internal capsule and the ventral fimbria, distinguished by higher T_2^* values and a difference in fiber orientations (Fig. 5).

Posterior commissure

The posterior commissure, forming a roof over the third ventricle at the boundary between the diencephalon and telencephalon, was delineated based on its low signal intensity in T_2^* -weighted images.

Facial nerve

The facial nerve (7th cranial nerve, Fig. 6G) and its ascending fibers were delineated based on FA maps, whereas the genu of the facial nerve was identified by its low intensity in T_2^* -weighted images.

Optic fiber system and supraoptic decussation

The optic nerve was delineated based on its low intensity in T_2^* -weighted images, aided by FA maps, from its origin in the retina to the level where the right and left optic nerves merge in the optic chiasm. The optic chiasm and tract were delineated together as one structure on basis of high FA values and DTI orientations. The optic tract was readily followed to the point where it adjoins the descending peduncle and curves laterally around the thalamus. The supraoptic decussation was distinguished from the optic tract and corticofugal pathways on the basis of high T_2^* -signal intensity (Fig. 5A), lower FA values and slightly different DTI fiber orientations (Fig. 5C).

Trigeminal nerve and spinal trigeminal tract

The sensory and motor roots of the trigeminal nerve and the spinal trigeminal tract were delineated together, readily distinguished by high FA values and distinct low T_2^* signal intensity. Diffusion orientations were used to differentiate the trigeminal nerve from the middle cerebellar peduncle, and T_2^* contrast was used to delineate the spinal trigeminal tract against the medially located spinal trigeminal nucleus. The spinal trigeminal tract was further differentiated from more externally located white matter tracts (inferior cerebellar peduncle,

trapezoid body, vestibulocochlear nerve) on basis of its distinct axial diffusion orientations (Figs. 4G–I).

White matter of the tectum

The commissures of the superior and inferior colliculi and the brachium of the superior colliculus were delineated on basis of distinct low T_2^* signal intensity, aided by high FA values and mediolateral DTI orientations.

Cerebellar and precerebellar white matter

The white matter of the cerebellum and the layered organization of the cerebellum were seen in both T_2^* and DTI maps (Figs. 4G–I). However, since the low intensity T_2^* signals of the cerebellar white matter were difficult to distinguish from the overlying granule cell layer (with medium intensity T_2^* signals) at several locations, we chose not to delineate the cerebellar white matter separately (see also the Cerebellum section, below). In the present version of the atlas the superior cerebellar peduncle was not delineated separately but included in the brain stem region. The middle and inferior cerebellar peduncles were delineated using primarily DTI maps, aided by the T_2^* -weighted images. The delineations were truncated at the level where the fiber tracts enter the cerebellum, arbitrarily defined by a line connecting the lateral corner of the 4th ventricle with the lateral recess of the 4th ventricle. The transverse fibers of the pons were delineated on the basis of low T_2^* and high FA values and identified as a continuous white matter layer covering the external surface of the pontine nuclei. The transition to the middle cerebellar peduncle was set where the fibers leave the surface of pontine nuclei.

Gray matter

Olfactory system

Within the olfactory and accessory olfactory bulb, the outer (glomerular) layers were separately delineated based on the substantially lower T_2^* signal intensity in these layers relative to the deeper layers. The deeper layers of the olfactory and accessory olfactory bulb, the lateral olfactory tract, and the anterior parts of the piriform cortex were delineated as one structure (Figs. 1A, A', B, B'), whereas the intrabulbar part of the anterior commissure was delineated separately (see the Anterior commissure section above). Posterior to the olfactory bulb, the olfactory system protrudes ventrally below the ventral pallidum and the orbital and insular cortices. Anteriorly, the olfactory system is divided from the cerebral cortex by the rhinal incisure and the rhinal fissure. In more posterior regions, where the rhinal fissure is shallow, the dorsal boundary of the olfactory system was delineated on basis of the lower T_2^* signal intensity observed in the ventral and lateral orbital cortex, and insular cortex, and further by the homogenous high T_2^* intensity seen in the accumbens nucleus. The piriform cortex, forming the most dorsolateral part of the olfactory system, was identified as a homogeneous region appearing relatively bright in T_2^* images, with its distinctly curving layer 2 clearly visible in diffusion weighted images (Figs. 1B'). The medial and ventromedial boundary of the olfactory system was defined against the navicular nucleus of the basal forebrain (with lower T_2^* intensity) and the ventral pallidum (with distinct anteroposterior fiber orientations). The olfactory tubercle, located medial to the lateral olfactory tract, could not be distinguished from the ventral pallidum and was therefore not included. Towards posterior, the delineation of the olfactory system was arbitrarily truncated at the anteroposterior

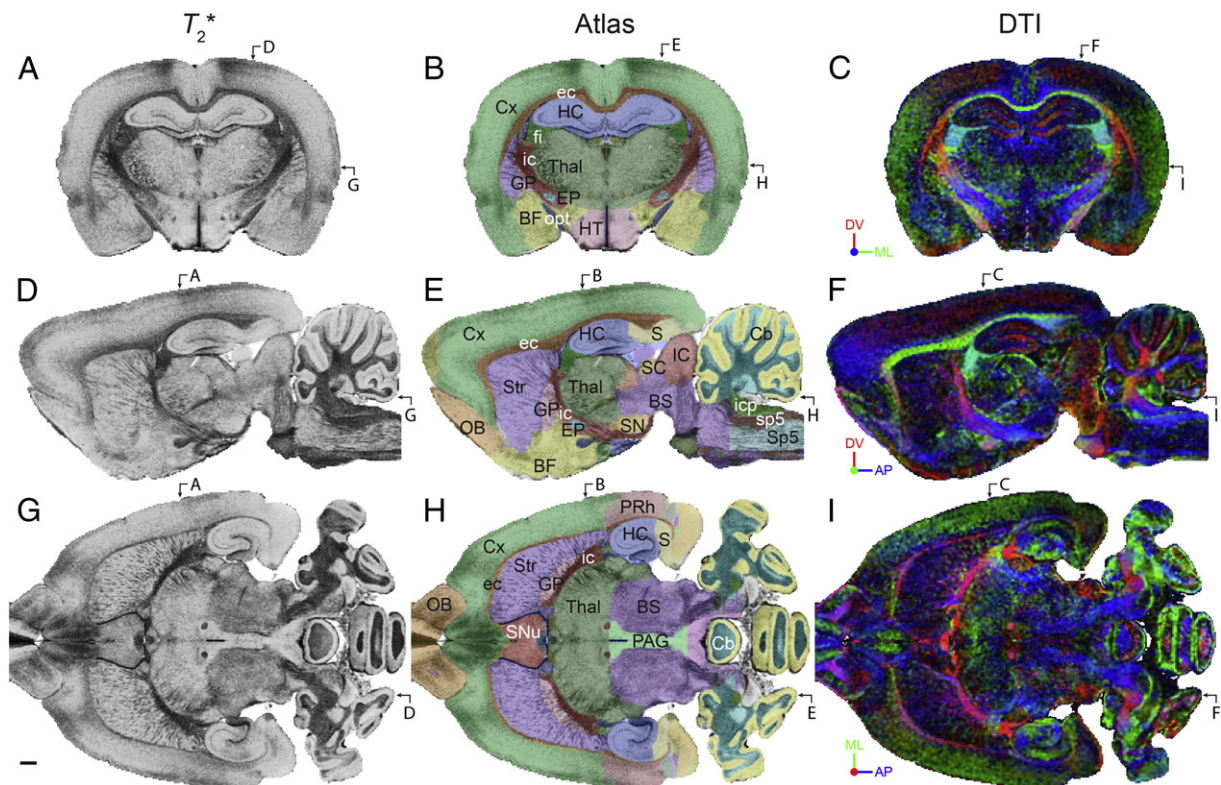


Fig. 4. Overview of anatomical features and delineations. Atlas delineations are shown in coronal, sagittal and horizontal views (B,E,H), together with corresponding T_2^* (A,D,G) and DT (C,F,I) images showing corresponding and complementary features. Arrows indicate the positions of the different image planes. Insets in C, F, and I show the RGB color code used for DTI orientation. BF, basal forebrain region; BS, brain stem; Cb, cerebellum; Cx, cerebral cortex; ec, external capsule; EP, entopeduncular nucleus; fi, fimbria; GP, globus pallidus; HC, hippocampal formation; HT, hypothalamic region; IC, inferior colliculus; ic, internal capsule; icp, inferior cerebellar peduncle; OB, olfactory bulb; opt, optic tract; PAG, periaqueductal gray; PRh, perirhinal cortex; S, subiculum; SC, superior colliculus; SN, substantia nigra; SNu, septal nuclei; Sp5, spinal trigeminal nucleus; sp5, spinal trigeminal tract; Str, striatum; Thal, thalamus. Scale bars: 1 mm.

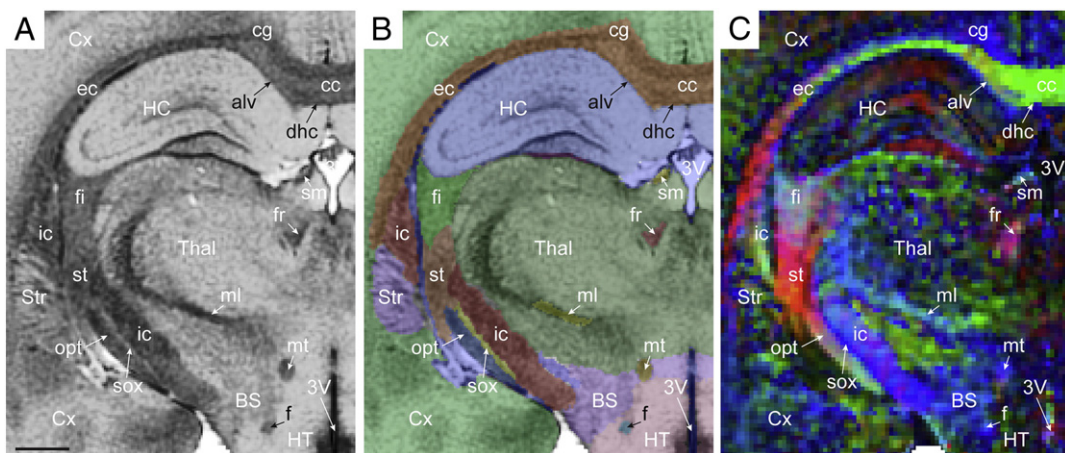


Fig. 5. Structural details in white and gray matter visible in corresponding T_2^* (A) and DTI (C) images, and with atlas delineations superimposed on the T_2^* image (B), from a coronal MRI slice through the hippocampus, thalamus, and hypothalamic region. 3V, third ventricle; alv, alveus; BS, brain stem region; cc, corpus callosum; cg, cingulum; Cx, cerebral cortex; dhc, dorsal hippocampal commissure; ec, external capsule; f, fornix; fi, fimbria; fr, fasciculus retroflexus; HC, hippocampal formation; HT, hypothalamic region; ic, internal capsule; ml, medial lemniscus; mt, mammillothalamic tract; opt, optic tract; sm, stria medullaris; sox, supraoptic decussation; st, stria terminalis; Str, striatum; Thal, thalamus. Scale bar: 1 mm.

level where the rhinal fissure becomes a shallow groove on the lateral surface of the cerebral cortex.

Cerebral cortex including the neocortex and the hippocampus

The label neocortex in the present atlas comprises all parts of the cerebral cortex not included in the olfactory system or in the hippocampal and parahippocampal regions (Figs. 4–6). Only the frontal association cortex and area 2 of the cingulate cortex were delineated as separate structures. The frontal association cortex was delineated based on slight differences in T_2^* contrast towards the orbital cortex and the secondary motor cortex, whereas area 2 of the cingulate cortex was outlined with use of white matter landmarks in the T_2^* -weighted images. Delineations of structures in the hippocampal and parahippocampal regions were taken from a parallel investigation of hippocampal boundaries in the

same MRI/DTI material (L.J. Kjonigsen, T.B. Leergaard, M.P. Witter, and J.G. Bjaalie, in preparation) based on criteria provided by Kjonigsen et al. (2011). The structures included were the entorhinal, perirhinal and postrhinal cortices of the parahippocampal region, the subiculum, and the remaining hippocampal formation (cornu ammonis regions 1–3, the fasciola cinereum, and the dentate gyrus, together labeled as hippocampal formation).

Striatum

The striatum, comprising the caudate–putamen complex and the core and shell of the accumbens nucleus (Gerfen, 2004), was distinguished by its distinct low FA signal intensity, in addition to contrast provided by surrounding structures (Figs. 1, 4D–I). The striatum is dorsally covered by white matter (the corpus callosum and external

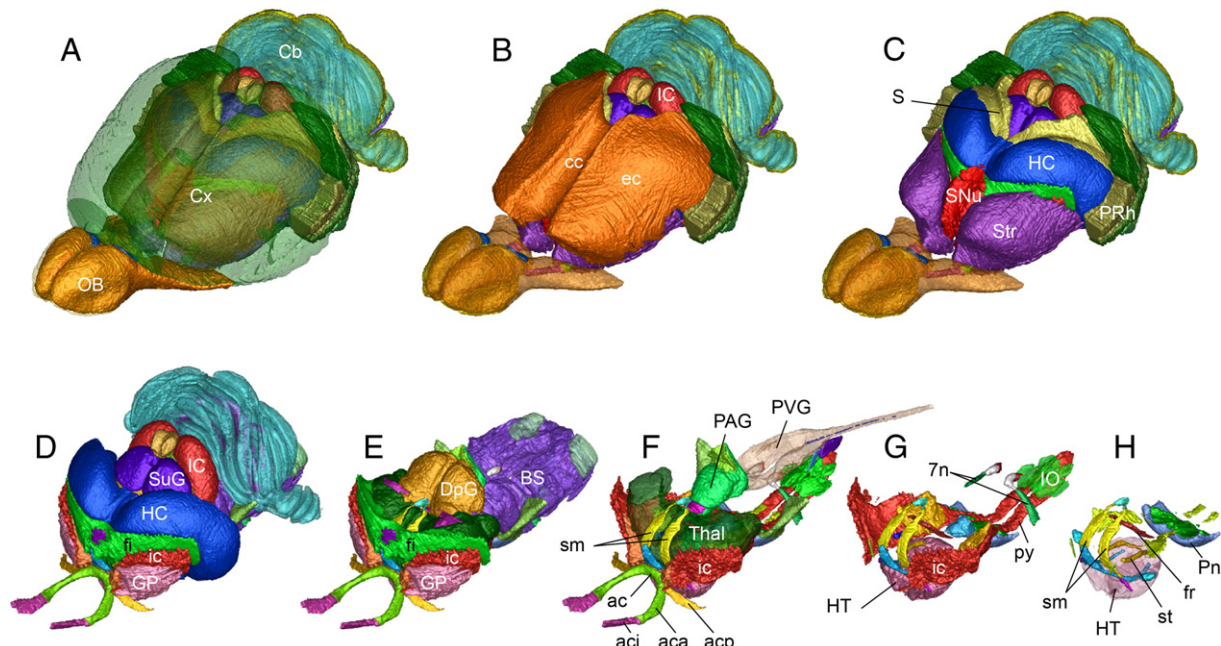


Fig. 6. Surface models of the Waxholm Space atlas of the Sprague Dawley rat brain, showing the 3D shape and position of selected structures. 7n, facial nerve; ac, anterior commissure; aca, anterior commissure, anterior part; aci, anterior commissure, intrabulbar part; acp, anterior commissure, posterior part; BS, brain stem; Cb, cerebellum; cc, corpus callosum; Cx, cerebral cortex; DpG, deep gray layer of the superior colliculus; ec, external capsule; fi, fimbria; fr, fasciculus retroflexus; GP, globus pallidus; HC, hippocampal formation; HT, hypothalamic region; IC, inferior colliculus; ic, internal capsule; OB, olfactory bulb; PAG, periaqueductal gray matter; PRh, perirhinal cortex; PVG, periventricular gray matter; py, pyramidal tract; S, subiculum; SC, superior colliculus; SuG, superficial gray layer of the superior colliculus; sm, stria medullaris; SNU, septal nuclei; st, stria terminalis; Str, striatum; Thal, thalamus.

capsule) with low T_2^* intensity and high anisotropy (Fig. 4). The anterior protrusion of the accumbens nucleus was delineated based on its low anisotropy and homogenous bright appearance in T_2^* images. The medial boundary of the anterior striatum is given mostly by the lateral ventricles (black/white in T_2^* -weighted images), in addition to the nacicular nucleus and anterior olfactory nucleus (with anteroposterior DTI orientations) and the septal nuclei (with slightly lower T_2^* intensity, and relatively higher anisotropy). Further posterior, the internal capsule (characterized by low T_2^* intensity, and high anisotropy) and the globus pallidus provide the medial/ventromedial boundary of the striatum. The anterior part of the striatum was delineated ventrally against the medial forebrain bundle and the ventral pallidum, both included in the basal forebrain region. The white matter of the medial forebrain bundle was easily identified by its low T_2^* signal intensity and high anisotropy (anteroposterior fiber orientations), while the rest of the ventral pallidum provides a boundary by its relatively higher anisotropy compared to the striatum, showing mostly anteroposterior diffusion orientations. Further posterior, the posterior limb of the anterior commissure (with distinct mediolateral fiber orientations) and the interstitial nucleus of the posterior limb of the anterior commissure (with relatively low T_2^* intensity) give the ventral boundary of the striatum. The lateral/ventrolateral extent of the striatum, which is not delimited by the external capsule, was delineated against the claustrum and the endopiriform nuclei (with darker T_2^* signals), and more posteriorly by the amygdaloid nuclei (with slightly darker, homogenous T_2^* contrast, lacking the typical striated appearance of the striatum).

Globus pallidus

The globus pallidus is readily distinguished medially from the white matter of the internal capsule by its bright T_2^* contrast. The dorsolateral boundary towards the striatum is more difficult to see in the T_2^* images since the overall appearance of the tissue is striated in both regions. The boundary is indicated by a thin band of slightly darker signal between the globus pallidus and the striatum (Figs. 1A'–D'; 4D,G), coinciding with a relatively sharp boundary given by higher FA values in the globus pallidus (Figs. 4F,I), corresponding to the higher density of fibers in this region. The anterior part of the globus pallidus is ventrally delimited partly by the posterior limb of the anterior commissure (with dark T_2^* signal, mediolateral fiber orientation) and the associated interstitial nucleus (with slightly brighter T_2^* signal), and partly by the ventral pallidum. The distinct appearance of the globus pallidus with high densities of fiber bundles was used to delineate its ventral boundary against the ventral pallidum (included in the basal forebrain region) and the substantia nigra extended amygdala, aided also by slightly darker T_2^* signal in the extended amygdala. The basal nucleus (of Meynert), intercalated between the globus pallidus and extended amygdala, was not possible to identify separately and was therefore included in the delineation of the globus pallidus. Further posterior, the globus pallidus is ventrally adjacent to the amygdaloid nuclei showing darker FA signals. The posterior border of the globus pallidus is given by the inferosuperior segment of the stria terminalis (identified by high FA values) directly posterior to the internal capsule and anteroventral to the fimbria.

Entopeduncular nucleus

The entopeduncular nucleus, a small gray matter region embedded in the internal capsule, is clearly visible as an island with bright T_2^* signal and reticular appearance surrounded by white matter (Figs. 4A,G). It is to some extent also visible as small fragments with reduced fractional anisotropy in the FA maps.

Subthalamic nucleus

The subthalamic nucleus is visible as a distinct island of bright T_2^* signal located dorsomedial to the cerebral peduncle, anterior to the substantia nigra, and ventral to the thalamus/zona incerta. The nucleus was delineated using both T_2^* , T_2 , and FA images. In T_2 and T_2^* images,

the subthalamic nucleus appears with bright signal, while in the FA image it appears as a dark region. As the T_2^* image shows significant distortions in this region on the right side, the other two image modalities were used for the delineation.

Basal forebrain region

The basal forebrain is a large complex of smaller regions located ventral to the striatum (Figs. 1, 4G,H, 5). In the current version of the atlas, the basal forebrain was provisionally defined as including brain regions located at the floor of the brain, between the olfactory system and hypothalamic region, inferior to the striatum and globus pallidus. For identification of boundaries, we refer to the delineation criteria for the surrounding structures (the olfactory bulb, the cerebellar cortex, the striatum and globus pallidus, the septal region, the ventricular system, the thalamus, and the hypothalamic region).

Septal region

Although the septal nuclei are often considered part of the basal forebrain (<http://neurolex.org/>), we have here delineated the septal region individually, defined as the region situated medially between the lateral ventricles, directly ventral to the corpus callosum, encompassing the anterior fornix, and separating the anterior hippocampal structures (the fimbria and the ventral hippocampal commissure) from the dorsal peduncular cortex. The septal region was distinguished from surrounding areas by its bright T_2^* contrast, low anisotropy, and distinctive blend of dorsoventral and anteroposterior tissue orientations. The ventral boundary of the septal region against the basal forebrain was approximated based on the same characteristics, aided by a slight shift towards brighter T_2^* signal in the basal forebrain.

Thalamus

For the present version of the atlas, we have delineated the thalamus as a single region without subdivisions, incorporating the main nuclear groups of the epithalamus, dorsal thalamus, and ventral thalamus (Jones, 2007). The delineation was aided by the identification of distinct white matter bundles surrounding and entering the thalamus (Figs. 6F–H; see the Thalamic tracts section above). The overall shape of the thalamus is most apparent in horizontal view (Figs. 4D–F). The round anterior surface of the thalamus is delimited towards lateral by the 3rd ventricle (with very bright T_2^* signal), the fornix, the stria medullaris, the bed nucleus of the stria terminalis, and the arc of the stria terminalis, and further lateral by the adjacent convex surface of the internal capsule and the fimbria of the hippocampus (white matter with darker T_2^* contrast), and the bed nucleus of the stria terminalis (with slightly brighter signal compared to the thalamus). The dorsal surface of the thalamus is bounded by the 3rd ventricle, the brachium of the superior colliculus, the stria medullaris of the thalamus, and the hippocampal formation (Fig. 5). The lateral boundary of the anterior thalamus is given by the internal capsule, the fimbria, and the arc of the stria terminalis intercalated between the two other white matter bundles. The posterior boundary of the thalamus is defined by the optic tract, the hippocampus, and the ventricular system. The ventral boundary of the anterior thalamus against the basal forebrain region was partly defined by the curvatures of the stria medullaris and fornix, and partly by the medial division of the bed nucleus of the stria terminalis, which appeared as a zone of bright T_2^* contrast surrounding the fornix (Fig. 5). The paraventricular hypothalamic nucleus, an area of dark T_2^* contrast tightly surrounding the ventral half of the 3rd ventricle, also contributes to this boundary. Further posteriorly, the ventrolateral boundary of the thalamus was identified using the noticeable dark shift in T_2^* contrast towards the basal forebrain in an arc extending the medial surface of the internal capsule in the ventromedial direction (Fig. 5). The ventral boundary of the anterior part of the thalamus towards the hypothalamic region was approximated by a curve following a zone with a slight drop in FA signal. From the level where the bed nucleus of the stria terminalis disappears and the medial magnocellular

nuclei become visible medially (elongated structures running obliquely dorsolateral from the 3rd ventricle towards posterior, with dark T_2^* signal), the zona incerta was used to define the ventral boundary of the thalamus towards the basal forebrain region.

The zona incerta can be considered a part of the ventral thalamus (Jones, 2007) and is here thus included as part of the thalamus. This region is intercalated between the white matter bundles of the internal capsule, the medial lemniscus, and the mammillothalamic tract, clearly defined by distinct mediolateral fiber orientations standing out against the oblique fiber orientations of the more laterally located internal capsule, and the low anisotropic values of the ventrally and medially located hypothalamic region (Fig. 5). Medially, between the zona incerta on each side, at level of the reunions thalamic nucleus and reunions area, the ventral extent of the thalamus was approximated on the basis of a reduction in fractional anisotropy towards the hypothalamic region. The posterior boundary of the thalamus was delineated against several mesencephalic structures. The pretectal nuclei appear dorsally as regions with slightly brighter T_2^* contrast and mediolateral tissue orientation, giving a round lateral surface against the horns of the thalamus, and a rather flat surface towards the dorsal half of the flattened concave part of the thalamic crescent. This boundary is best seen and thus approximated in horizontal view. At the dorsoventral midline of the posterior surface of the thalamus, it meets the periaqueductal gray (with brighter T_2^* signals), at the anteroposterior level where the dorsal and ventral parts of the 3rd ventricle join. The fasciculus retroflexus (with very dark T_2^* signals, and inferosuperior DTI orientations) and the surrounding parafascicular nucleus (having brighter T_2^* signals compared to the thalamus, and slightly darker T_2^* signals than the periaqueductal gray matter) also contribute to this boundary up to the posterior level where the periaqueductal gray appears medially between the right and left fasciculus retroflexus. The ventral half of the crescent is delimited by the tectal part of the reticular formation (included in the brain stem), showing considerably darker T_2^* contrast and characteristic reticular tissue structure picked up in the MRI. It should be noted that the right side of the MR image shows severe distortions at the posterior parts of the thalamus, and therefore the posterior boundary on this side was largely approximated to be symmetrical to the left side.

Bed nucleus of the stria terminalis

The bed nucleus of the stria terminalis was identified as a zone of relatively bright T_2^* signals located posterior to striatum, between the anterior commissure, septal region, internal capsule and the lateral ventricle. The lateral and medial boundaries of the anterior part of the region are given by the internal capsule and the septal region, respectively. Posterior to the level where the 3rd ventricle merges with the lateral ventricles, the bed nucleus of the stria terminalis is medially delimited by the anterior thalamus (paratenial nucleus, with slightly darker T_2^* signal), the stria medullaris (with high FA and dorsoventral DTI orientations), and the fornix (with oblique anteroposterior and dorsoventral diffusion orientations). Its dorsomedial boundary is given by the lateral ventricle, whereas its dorsolateral boundary is adjacent to the stria terminalis (with bright FA signals). Complementing the arc formed by the stria terminalis and the dorsal part of its bed nucleus, the ventral extension of the bed nucleus of the stria terminalis encompasses the anterior side of the fornix, appearing as a curved zone of bright T_2^* signal surrounding the fornix. The bed nucleus of the stria terminalis can be followed towards posterior along the fornix to the level where the fornix becomes detached from the thalamic surface.

Nucleus of the stria medullaris

The nucleus of the stria medullaris appears as a ventrolateral extension of the stria medullaris at the level where the stria medullaris emerges below the dorsal and anterior surface of the thalamus. The nucleus is readily distinguished from the stria medullaris (which has darker T^* contrast) and from the basal forebrain region (which has brighter T_2^* contrast).

Hypothalamic region

The hypothalamus contains several smaller nuclei, some of which can be recognized in the image material (e.g. the paraventricular and the periventricular nuclei, and the pars compacta of the dorsomedial hypothalamic nucleus). These regions are not separately delineated in the present version of the atlas. The hypothalamic region is characterized by low anisotropy compared to the surrounding regions (Fig. 5). Its dorsal and ventral extents are mostly given by the thalamus, the brain stem, and the ventral brain surface. The optic chiasm and optic tract, as well as the supraoptic decussation (all with very bright FA signal) also contribute to the ventral and ventrolateral boundary. The lateral dimensions of the hypothalamic region, where not defined by the outer brain surface, were approximated against the slightly darker T_2^* signal and higher anisotropy of the basal forebrain region. The more posteriorly located peduncular part of the lateral hypothalamus is here not identified separately, but rather included in the basal forebrain region. The fornix and the surrounding bed nucleus of the stria terminalis contribute further to this lateral boundary. Similarly, the anterior part of the hypothalamus was estimated as a zone of bright T_2^* contrast located between the optic chiasm, the medial division of the bed nucleus of the stria terminalis, and the preoptic area (included in the basal forebrain region). Directly posterior to the level where the mammillothalamic tract is located between the thalamus and the hypothalamus, the dorsal/dorsolateral border of the hypothalamic region is given by the protruding reticular formation (characterized by darker T_2^* signal with characteristic reticular pattern, here delineated as part of the brain stem) and medially by the periaqueductal gray. Due to the lack of contrast between the posterior hypothalamic area and the periaqueductal gray, this boundary was set to follow the ventral surface of the mammillothalamic tract. The most posterior part of the hypothalamic region is formed by the mammillary nuclei (with brighter T_2^* contrast).

Pineal gland

Anterolaterally, the dorsal half of the pineal gland is adjacent to the cortex, separated by a clear boundary and distinguished also by its brighter T_2^* contrast. Otherwise the boundaries of the pineal gland are readily given by the saturated or zero signal (depending on the presence of contrast agent) in the surrounding cerebrospinal fluid.

Tectum

The tectum was parcellated into the superficial and deep layers of the superior colliculus, the inferior colliculus and the commissure of the inferior colliculus. The region between the thalamus and superior colliculus (containing several pretectal nuclei) was delineated as the pretectal region. The superficial gray layer of the superior colliculus was readily identified as a zone of bright T_2^* contrast located between the brain surface and the deeper layers of the superior colliculus. The deeper layers of the superior colliculus (including the optic nerve layer, and the intermediate and deep gray and white layers) were here collectively delineated. The posterior boundary of the superior colliculus was set at the level of the groove separating the superior gray layer from the inferior colliculus, and given by the homogeneous T_2^* appearance of the inferior colliculus and the commissure of the inferior colliculus. The anterior boundary of the superior colliculus was more difficult to distinguish from the pretectal nuclei, but was approximated by observing zones with subtle alternating differences in T_2^* contrast, probably reflecting the different layers of the superior colliculus. The ventral boundary of the superior colliculus against the reticular formation was delineated using the distinct mediolateral diffusion orientations in the deep layers of the superior colliculus, aided also by slightly darker T_2^* signal and the characteristic reticular appearance of tissue in the reticular formation. The ventromedial boundary of the superior colliculus was difficult to see in DTI, and was approximated by following a wedge-shaped area with brighter T_2^* signals presumably reflecting the precuneiform area.

The dorsal cap of the inferior colliculus was defined by the brain surface and its posterior boundary was given by the precerebellar fissure. The gray matter of the inferior colliculus was identified as a large ovoid shaped area with brighter T_2^* signal than the surrounding precuneiform area and reticular formation. The ventral boundary of the inferior colliculus was clearly demarcated by the high FA and dorsoventral diffusion orientations of the lateral lemniscus, and more subtle differences in T_2^* signal and DTI orientations in the precuneiform area. The medial boundary of the inferior colliculus is given by the commissure of the inferior colliculus, the periaqueductal gray matter, and the 4th ventricle.

Substantia nigra

The substantia nigra was delineated as a single structure without subdivisions. The lateral and ventral boundaries of the structure are readily given by the cerebral peduncle (with dark T_2^* signal and high FA; Figs. 4G–I), while the dorsal and medial boundaries are more difficult to see. We interpreted a thin zone with slightly darker T_2^* contrast to reflect the somewhat higher cell density of the compact part of the substantia nigra and included this in the dorsomedial boundary of the substantia nigra. This boundary partly overlaps with the mediolaterally oriented diffusion orientations located ventral to the medial lemniscus, presumably reflecting fibers emerging from the dorsal part of the substantia nigra.

Interpeduncular nucleus

The interpeduncular nucleus was readily distinguished from the brain stem based on its bright T_2^* signal and homogenous and compact appearance, as well as its position ventral to the brain stem and rostral to the pontine nuclei.

Periaqueductal gray

The periaqueductal gray was delineated on the basis of T_2^* contrast. The anterior boundary was identified on basis of the darker T_2^* signals observed in the thalamus (see the Thalamus section above). In coronal slices, the periaqueductal gray was clearly visible as a region of bright T_2^* contrast surrounding the aqueduct (Figs. 4D,E). The posterior end of the periaqueductal gray and transition to the different tegmental nuclei surrounding the 4th ventricle (here included in the brain stem region) was set at the most anterior level of the cerebellum (where the 2nd lobule protrudes into the 4th ventricle).

Pontine nuclei

The pontine nuclei were delineated based on their bright T_2^* signal and their unique position ventral to the brain stem. The present delineation includes the pontine gray matter located ventral to the descending longitudinal fasciculus of the pons and partly surrounding it. The transverse fibers of the pons and the middle cerebellar peduncles were delineated separately.

Cerebellum

The high-resolution T_2^* images and DT images provided much structural detail in the cerebellum (Figs. 4G–I), but we here only subdivided the cerebellum into the molecular cell layer (with very bright T_2^* contrast) and the deeper cerebellum, which included the Purkinje cell layer, granule cell layer, white matter, and deep cerebellar nuclei. The cerebellum was divided from the rest of the brain by extrapolating the surface of the brain stem through the superior, middle, and inferior cerebellar peduncles. At some levels we used an imaginary line connecting the lateral corner of the 4th ventricle and the lateral recess of the 4th ventricle as a guideline.

Inferior olive

The inferior olfactory complex was delineated based on its bright T_2^* signal and distinct shape. The distinct mediolateral diffusion orientations

in the inferior olive further aided delineation against the anteroposterior diffusion orientations in the pyramidal tracts.

Spinal trigeminal nucleus

The spinal trigeminal nucleus was delineated based on its fairly bright signal and striated appearance caused by axially oriented fibers with dark T_2^* signal. The spinal trigeminal tract (with distinct dark T_2^* signals) delimits the spinal trigeminal nucleus laterally and to a certain extent also dorsally and ventrally. The medial boundary of the spinal trigeminal nucleus was identified on basis of the slightly brighter T_2^* signals in this region. The principal trigeminal nucleus was not delineated here, and the anterior boundary of the spinal trigeminal nucleus was arbitrarily set at the level where the facial nerve exits the brain stem, while the posterior boundary was set at the coronal level of the pyramidal decussation.

Gray matter in the floor of the 4th ventricle and surrounding the central canal

The gray matter found in the continuation of the periaqueductal gray, adjacent to the floor of the 4th ventricle and surrounding the central canal, was delineated as a continuous structure based on its bright T_2^* contrast.

Brain stem

In the present atlas, the region *brain stem* includes all otherwise unlabeled areas of the midbrain, the pons, and the medulla oblongata. Accordingly, this region incorporates the reticular formation and several nuclei. The anterior boundary of the region is given by the thalamus and hypothalamic region. It is divided medially by the periaqueductal gray and limited dorsally by the tectum and the periaqueductal gray. The ventral borders are given by the descending pathways (cerebral peduncle and pyramidal tract), the substantia nigra, the interpeduncular nucleus, the pontine nuclei (with bright T_2^* signal), the transverse fibers of the pons (high FA values), and the trapezoid body (dark T_2^* signal). Further, at the level of the pons, the region is framed laterally by the middle cerebellar peduncle (relatively homogenous dark T_2^* signal, dorsoventral diffusion orientation) and the spinal trigeminal tract (very dark T_2^* signal, distinct anteroposterior DTI signal). In the medulla oblongata, the dorsal boundary is defined by the 4th ventricle and the gray matter adjacent to its floor (bright T_2 and T_2^* signal), as well as by the cerebellum. The lateral boundary at this level is defined by the inferior cerebellar peduncle and the spinal trigeminal tract, both distinguished based on DTI. Ventral borders are given by the trapezoid body (mediolateral fiber orientation) and the medial lemniscus (anteroposterior fiber orientation), and further on by the inferior olive (bright T_2^* signal and distinct shape and orientation). Posterior to the facial nerve, the region is delimited by the spinal trigeminal nuclei appearing laterally (brighter T_2^* signal and dotted appearance). Approaching the spinal cord, the brain stem again has a direct contact with the descending pathway/pyramidal tracts. The posterior boundary of the region is given by the spinal cord.

Ventricular system

The ventricular system (comprising the lateral ventricles, 3rd ventricle, aqueduct, and 4th ventricle) was delineated as a single structure based on the nearly saturated bright signal in T_2 -weighted and T_2^* -weighted images, reflecting the presence of the contrast agent used in this preparation. The same signal was used to delineate the medullary and cervical central canal as a separate structure, starting at the obex and extending towards posterior in the whole length of the spinal cord delineation. Since the ventricular system is continuous with further spaces filled with cerebrospinal fluid surrounding the brain, arbitrary boundaries were placed 1) at the anterior level where the pineal gland first appears in the coronal view, 2) at the posterior level where the pineal gland no longer touches the cerebral cortex on either side

in the coronal view, and 3) at the posterior level where the horns of the thalamus (geniculate nuclei) disappear from the coronal view.

Spinal cord

The spinal cord was defined as starting at the last coronal level showing the occipital bone. The spinal cord was delineated approximately 8.62 mm posterior to the skull until leaving the field of view. The outer boundaries of the spinal cord were identified using bright T_2 and T_2^* signal originating from the cerebrospinal fluid in the subarachnoid space. The central canal and the surrounding gray matter, as well as fibers extending from the descending pathways, were delineated separately.

Discussion

The key results of the present study are fourfold. First, we have produced a microscopic resolution isotropic MRI and DTI template for the Sprague Dawley rat brain. Second, on the basis of this template we have built an atlas of major anatomical structures in the brain, and we provide detailed delineation criteria for all structures in this atlas. Third, we have applied a spatial reference system based on internal brain landmarks according to the Waxholm Space standard, previously developed for the mouse brain. Fourth, we have connected this spatial reference system to the widely used stereotaxic coordinate system by identifying cranial sutures and related stereotaxic landmarks in the template using contrast given by the active staining technique applied to the tissue. With the release of the present atlasing template and parcellations, we provide a new tool for spatial orientation in analysis of neuroanatomical location and planning and guidance of experimental procedures in the rat brain.

The atlas is based on contrast enhanced ex vivo MRI acquired using a protocol that minimizes morphological distortions by gentle perfusion and by imaging the brain *in situ* within the cranium (Badea et al., 2007; for comparison with *in vivo* imaging, see also Benveniste et al., 2007). It is thus reasonable to assume that tissue fixation has not introduced any major morphological differences in our ex vivo template as compared to the *in vivo* brain, at least not at a level exceeding distortions that may occur in histological material. Further, the high spatial resolution and structural contrast obtained in our ex vivo images greatly facilitate the identification of anatomical landmarks and delineation of smaller anatomical regions that would not be visible in *in vivo* MRI with larger voxel size. Partial volume effects by inclusion of surrounding tissues are also reduced by the small voxel size. It should be noted that the properties of water diffusion are altered in fixed tissues, such that the diffusion parameters in the present data are altered from the *in vivo* situation, but with relevant diffusion orientations (D'Arceuil and de Crespigny, 2007; Sun et al., 2003, 2005). Earlier rat brain atlasing studies have transferred delineations from existing histological atlases to MRI templates at various levels of granularity. Such atlases have provided useful results in context of functional (Nie et al., 2013) and pharmacological (Schwarz et al., 2006) neuroimaging, and analyses of tissue contrast (Johnson et al., 2012). Veraart et al. (2011) used a different atlasing approach by delineating anatomical regions directly based on anatomical MRI and DTI in selected regions of the brain. Our work expands this concept to the whole brain level.

Semi-automatic segmentation of MRI data with the aim of identifying anatomical regions is based on image intensity and contrast, and manual detection of signal changes at locations corresponding to known anatomical boundaries. Changes in intensity and contrast are known to reflect changes in cell and fiber densities (see, e.g. Alexander et al., 2007; Malisch et al., 1991; Norris et al., 2013). But since MRI does not provide the same high level of specificity as histology, transitions in signal contrast and intensity were only recorded as boundaries if located in agreement with corresponding histologically defined boundaries, as shown in Paxinos and Watson (2007) or other literature

on brain anatomy (see the [Results](#) section). Delineation of anatomical boundaries in the present atlas therefore required substantial manual segmentation efforts. More than 40 million voxels containing structural information about the brain were assigned anatomical label using 2D and 3D segmentation (with brush diameters ranging from 1 to 88 voxels) by visual interpretation of image features in multiple semi-transparent layers (T_2 , T_2^* , FA, DTI maps) in three orientation planes (coronal, sagittal, and horizontal) while taking into consideration the available atlases and literature. Future datasets registered to our template can, however, be subject to "atlas-based" segmentation enabling the use of automated routines (see, e.g., Cabezas et al., 2011), as well as the generation of a population averaged template (Veraart et al., 2011).

Atlases are important tools for comparing and analyzing data, and a cornerstone for reaching out to diverse resources containing different types of information about the brain lies in the interoperability of the spatial reference systems used. We have implemented Waxholm Space in our rat brain template, and coupled the template to the stereotaxic skull based coordinate system (Paxinos and Watson, 1982), thereby facilitating translation of Waxholm Space to a variety of existing atlases operating in stereotaxic space. Interoperability and translation between atlases are in the mouse brain managed by a digital atlasing infrastructure developed by the International Neuroinformatics Coordinating Facility (INCF, Hawrylycz et al., 2009, 2011). Principles and components made available through this infrastructure are equally suitable and relevant for the rat brain.

A brain atlas is never complete or finalized. It can always be further improved and made more precise. First, the work presented here contains a relatively robust parcellation of 76 structures, but may well, at several locations, be subject to different interpretations of boundaries. Second, current ongoing more detailed 3D parcellation of the hippocampal region of the same atlas template demonstrates the potential for further refinement and development of the atlas as a region by region community effort (Papp et al., 2013). Third, the present atlas template represents a necessary starting point for creation of population based probabilistic atlases based on ex vivo or *in vivo* MRI data from additional animals. Other future challenges include further improving the understanding of how MRI contrast correlates to histological measures and establishing similar atlas resources for developmental stages.

We provide open access to the presented high resolution template and the accompanying atlas. The significance of open access is partly in the validation, further improvement and expansion of the atlas and partly in providing an atlas that can be freely used with various informatics tools, facilitating for example data analysis with anchoring of experimental data from histology or electrophysiology to atlas space.

Acknowledgments

We thank the INCF committee on digital brain atlasing for valuable discussions, Christopher Coello and Gergely Csics for expert technical assistance, and Sveinung Lillehaug for assistance with anatomical delineations. This work was supported by grants from the Research Council of Norway and the EC Human Brain Project to J.G.B. MRI imaging was performed at the Duke Center for In Vivo Microscopy, a NIH/NCRR National Biomedical Technology Research Center (P41 EB015897, to G.A.J.) and Small Animal Imaging Resource Program (U24 CA092656, to G.A.J.).

References

- Aggarwal, M., Zhang, J., Miller, M.I., Sidman, R.L., Mori, S., 2009. Magnetic resonance imaging and micro-computed tomography combined atlas of developing and adult mouse brains for stereotaxic surgery. *Neuroscience* 162, 1339–1350.
- Aggarwal, M., Zhang, J., Mori, S., 2011. Magnetic resonance imaging-based mouse brain atlas and its applications. *Methods Mol. Biol.* 711, 251–270.
- Alexander, A.L., Lee, J.E., Lazar, M., Field, A.S., 2007. Diffusion tensor imaging of the brain. *Neurotherapeutics* 4, 316–329.

- Badea, A., Ali-Sharief, A.A., Johnson, G.A., 2007. Morphometric analysis of the C57BL/6J mouse brain. *NeuroImage* 37, 683–693.
- Benveniste, H., Ma, Y., Dhawan, J., Gifford, A., Smith, S.D., Feinstein, I., Du, C., Grant, S.C., Hof, P.R., 2007. Anatomical and functional phenotyping of mice models of Alzheimer's disease by MR microscopy. *Annals of the New York Academy of Sciences* 1097, 12–29.
- Bjaalie, J.G., Papp, E.A., Kjonigsen, L.J., Johnson, G.A., Witter, M.P., Leergaard, T.B., 2013. Waxholm Space atlas of the rat brain with detailed hippocampal subdivisions. *Ann. Meet. Soc. Neurosci.*, San Diego.
- Cabezas, M., Oliver, A., Llado, X., Freixenet, J., Cuadra, M.B., 2011. A review of atlas-based segmentation for magnetic resonance brain images. *Comput. Methods Prog. Biomed.* 104, e158–e177.
- Chuang, N., Mori, S., Yamamoto, A., Jiang, H., Ye, X., Xu, X., Richards, L.J., Nathans, J., Miller, M.I., Toga, A.W., Sidman, R.L., Zhang, J., 2011. An MRI-based atlas and database of the developing mouse brain. *NeuroImage* 54, 80–89.
- D'Arceuil, H., de Crespigny, A., 2007. The effects of brain tissue decomposition on diffusion tensor imaging and tractography. *NeuroImage* 36, 64–68.
- Evans, A.C., Janke, A.L., Collins, D.L., Baillet, S., 2012. Brain templates and atlases. *NeuroImage* 62, 911–922.
- Franklin, K.B.J., 1997. The Mouse Brain: In Stereotaxic Coordinates, 1st ed. Academic Press.
- Gerfen, C.R., 2004. Basal ganglia. In: Paxinos, G. (Ed.), *The Rat Nervous System*. Elsevier Academic Press, San Diego.
- Gloor, P., 1955. Electrophysiological studies on the connections of the amygdaloid nucleus in the cat. I. The neuronal organization of the amygdaloid projection system. *Electroencephalogr. Clin. Neurophysiol.* 7, 223–242.
- Hawrylycz, M., Boline, J., Burger, A., Hashikawa, T., Johnson, G., Martone, M., Ng, L., Nissanov, J., Puelles, L., Ruffins, S., Verbeek, F., Zaslavsky, I., 2009. The INCF Digital Atlasing Program: Report on Digital Atlasing Standards in the Rodent Brain.
- Hawrylycz, M., Baldock, R.A., Burger, A., Hashikawa, T., Johnson, G.A., Martone, M., Ng, L., Lau, C., Larson, S.D., Nissanov, J., Puelles, L., Ruffins, S., Verbeek, F., Zaslavsky, I., Boline, J., 2011. Digital atlasing and standardization in the mouse brain. *PLoS Comput. Biol.* 7, e1001065.
- Jiang, Y., Johnson, G.A., 2010. Microscopic diffusion tensor imaging of the mouse brain. *NeuroImage* 50, 465–471.
- Johnson, G.A., Cofer, G.P., Gewalt, S.L., Hedlund, L.W., 2002. Morphologic phenotyping with MR microscopy: the visible mouse. *Radiology* 222, 789–793.
- Johnson, G.A., Ali-Sharief, A., Badea, A., Brandenburg, J., Cofer, G., Fubara, B., Gewalt, S., Hedlund, L.W., Upchurch, L., 2007. High-throughput morphologic phenotyping of the mouse brain with magnetic resonance histology. *NeuroImage* 37, 82–89.
- Johnson, G.A., Badea, A., Brandenburg, J., Cofer, G., Fubara, B., Liu, S., Nissanov, J., 2010. Waxholm space: an image-based reference for coordinating mouse brain research. *NeuroImage* 53, 365–372.
- Johnson, G.A., Calabrese, E., Badea, A., Paxinos, G., Watson, C., 2012. A multidimensional magnetic resonance histology atlas of the Wistar rat brain. *NeuroImage* 62, 1848–1856.
- Jones, E.G., 2007. The Thalamus, 2nd ed. Cambridge University Press, Cambridge.
- Kjonigsen, L.J., Leergaard, T.B., Witter, M.P., Bjaalie, J.G., 2011. Digital atlas of anatomical subdivisions and boundaries of the rat hippocampal region. *Front. Neuroinformatics* 5, 2.
- Kovacevic, N., Henderson, J.T., Chan, E., Lifshitz, N., Bishop, J., Evans, A.C., Henkelman, R.M., Chen, X.J., 2005. A three-dimensional MRI atlas of the mouse brain with estimates of the average and variability. *Cereb. Cortex* 15, 639–645.
- Le Bihan, D., Mangin, J.F., Poupon, C., Clark, C.A., Pappata, S., Molko, N., Chabriat, H., 2001. Diffusion tensor imaging: concepts and applications. *J. Magn. Reson. Imaging* 13, 534–546.
- Lee, D., Ruffins, S., Ng, Q., Sane, N., Anderson, S., Toga, A., 2010. MBAT: a scalable informatics system for unifying digital atlasing workflows. *BMC Bioinforma.* 11, 608.
- Leergaard, T.B., White, N.S., de Crespigny, A., Bolstad, I., D'Arceuil, H., Bjaalie, J.G., Dale, A.M., 2010. Quantitative histological validation of diffusion MRI fiber orientation distributions in the rat brain. *PLoS One* 5, e8595.
- Lein, E.S., Hawrylycz, M.J., Ao, N., Ayres, M., Bensinger, A., Bernard, A., Boe, A.F., Boguski, M.S., Brockway, K.S., Byrnes, E.J., Chen, L., Chen, L., Chen, T.M., Chin, M.C., Chong, J., Crook, B.E., Czaplinski, A., Dang, C.N., Datta, S., Dee, N.R., Desaki, A.L., Desta, T., Diep, E., Dolbarte, T.A., Donelan, M.J., Dong, H.W., Dougherty, J.G., Duncan, B.J., Ebbert, A.J., Eichele, G., Estin, L.K., Faber, C., Facer, B.A., Fields, R., Fischer, S.R., Fliss, T.P., Frensel, C., Gates, S.N., Glattfelder, K.J., Halverson, K.R., Hart, M.R., Hohmann, J.G., Howell, M.P., Jeung, D.P., Johnson, R.A., Karr, P.T., Kawai, R., Kidney, J.M., Knapik, R.H., Kuan, C.L., Lake, J.H., Laramee, A.R., Larsen, K.D., Lau, C., Lemon, T.A., Liang, A.J., Liu, Y., Luong, L.T., Michaels, J., Morgan, J.J., Morgan, R.J., Mortrud, M.T., Mosqueda, N.F., Ng, L.L., Ng, R., Orta, G.J., Overly, C.C., Pak, T.H., Parry, S.E., Pathak, S.D., Pearson, O.C., Puchalski, R.B., Riley, Z.L., Rockett, H.R., Rowland, S.A., Royall, J.J., Ruiz, M.J., Sarno, N.R., Schaffnit, K., Shapovalova, N.V., Sivisay, T., Slaughterbeck, C.R., Smith, S.C., Smith, K.A., Smith, B.I., Sodt, A.J., Stewart, N.N., Stumpf, K.R., Sunkin, S.M., Sutram, M., Tam, A., Teemer, C.D., Thaller, C., Thompson, C.L., Varnam, L.R., Visel, A., Whitlock, R.M., Wohlnoutka, P.E., Wolkey, C.K., Wong, V.Y., Wood, M., Yaylaoglu, M.B., Young, R.C., Youngstrom, B.L., Yuan, X.F., Zhang, B., Zwinger, T.A., Jones, A.R., 2007. Genome-wide atlas of gene expression in the adult mouse brain. *Nature* 445, 168–176.
- Lu, H., Scholl, C.A., Zuo, Y., Demny, S., Rea, W., Stein, E.A., Yang, Y., 2010. Registering and analyzing rat fMRI data in the stereotaxic framework by exploiting intrinsic anatomical features. *Magn. Reson. Imaging* 28, 146–152.
- Ma, Y., Hof, P.R., Grant, S.C., Blackband, S.J., Bennett, R., Slatate, L., McGuigan, M.D., Benveniste, H., 2005. A three-dimensional digital atlas database of the adult C57BL/6J mouse brain by magnetic resonance microscopy. *Neuroscience* 135, 1203–1215.
- Ma, Y., Smith, D., Hof, P.R., Foerster, B., Hamilton, S., Blackband, S.J., Yu, M., Benveniste, H., 2008. In vivo 3D digital atlas database of the adult C57BL/6J mouse brain by magnetic resonance microscopy. *Front. Neuroanat.* 2, 1.
- Mai, J.K., Paxinos, G., Voss, T., 2007. *Atlas of the Human Brain*, 3rd ed. Academic Press.
- Malisch, T., Hedlund, L.W., Suddarth, S.A., Johnson, G.A., 1991. MR microscopy at 7 T: effects of brain iron. *J. Magn. Reson. Imaging* 1, 301–305.
- Martin, R.F., Bowden, D.M., 2000. *Primate Brain Maps: Structure of the Macaque Brain*. Elsevier Science Limited.
- Morgane, P.J., Galler, J.R., Mokler, D.J., 2005. A review of systems and networks of the limbic forebrain/limbic midbrain. *Prog. Neurobiol.* 75, 143–160.
- Mukherjee, P., Berman, J.I., Chung, S.W., Hess, C.P., Henry, R.G., 2008. Diffusion tensor MR imaging and fiber tractography: theoretic underpinnings. *AJNR Am. J. Neuroradiol.* 29, 632–641.
- Nie, B., Chen, K., Zhao, S., Liu, J., Gu, X., Yao, Q., Hui, J., Zhang, Z., Teng, G., Zhao, C., Shan, B., 2013. A rat brain MRI template with digital stereotaxic atlas of fine anatomical delineations in Paxinos space and its automated application in voxel-wise analysis. *Hum. Brain Mapp.* 34, 1306–1318.
- Nieman, B.J., Flenniken, A.M., Adamson, S.L., Henkelman, R.M., Sled, J.G., 2006. Anatomical phenotyping in the brain and skull of a mutant mouse by magnetic resonance imaging and computed tomography. *Physiol. Genomics* 24, 154–162.
- Norris, F.C., Betts-Henderson, J., Wells, J.A., Cleary, J.O., Siow, B.M., Walker-Samuel, S., McCue, K., Salomoni, P., Scambler, P.J., Lythgoe, M.F., 2013. Enhanced tissue differentiation in the developing mouse brain using magnetic resonance micro-histology. *Magn. Reson. Med.* 70, 1380–1388.
- Papp, E.A., Kjonigsen, L.J., Lillehaug, S., Johnson, G.A., Witter, M.P., Leergaard, T.B., Bjaalie, J.G., 2013. Volumetric Waxholm Space atlas of the rat brain for spatial integration of experimental image data. *Front. Neuroinform. Conference Abstract: Neuroinformatics 2013*. <http://dx.doi.org/10.3389/conf.nfnf.2013.09.00003>.
- Paxinos, G., Franklin, K.B.J., 2012. *The Mouse Brain in Stereotaxic Coordinates*, 4th ed. Elsevier.
- Paxinos, G., Watson, C., 1982. *The Rat Brain in Stereotaxic Coordinates*. Academic Press, Sydney.
- Paxinos, G., Watson, C., 2007. *The Rat Brain in Stereotaxic Coordinates*, 6th ed. Elsevier.
- Paxinos, G., Huang, X., Toga, A.W., 1999. The Rhesus Monkey Brain in Stereotaxic Coordinates, 1st ed. Academic Press.
- Rumple, A., McMurry, M., Johns, J., Lauder, J., Makam, P., Radcliffe, M., Oguz, I., 2013. 3-dimensional diffusion tensor imaging (DTI) atlas of the rat brain. *PLoS One* 8, e67334.
- Schwarz, A.J., Danckaert, A., Reese, T., Gozzi, A., Paxinos, G., Watson, C., Merlo-Pich, E.V., Bifone, A., 2006. A stereotaxic MRI template set for the rat brain with tissue class distribution maps and co-registered anatomical atlas: application to pharmacological MRI. *NeuroImage* 32, 538–550.
- Schweinhardt, P., Fransson, P., Olson, L., Spenger, C., Andersson, J.L., 2003. A template for spatial normalisation of MR images of the rat brain. *J. Neurosci. Methods* 129, 105–113.
- Sun, S.W., Neil, J.J., Song, S.K., 2003. Relative indices of water diffusion anisotropy are equivalent in live and formalin-fixed mouse brains. *Magn. Reson. Med.* 50, 743–748.
- Sun, S.W., Song, S.K., Harms, M.P., Lin, S.J., Holtzman, D.M., Merchant, K.M., Kotyk, J.J., 2005. Detection of age-dependent brain injury in a mouse model of brain amyloidosis associated with Alzheimer's disease using magnetic resonance diffusion tensor imaging. *Exp. Neurol.* 191, 77–85.
- Swanson, L., 1992. *Brain Maps: Structure of the Rat Brain*. Elsevier, Amsterdam.
- Swanson, L., 2004. *Brain Maps: Structure of the Rat Brain*, 3rd ed. Elsevier, Amsterdam.
- Toga, A.W., Thompson, P.M., Mori, S., Amunts, K., Zilles, K., 2006. Towards multimodal atlases of the human brain. *Nat. Rev. Neurosci.* 7, 952–966.
- Valdes-Hernandez, P.A., Sumiyoshi, A., Nonaka, H., Haga, R., Aubert-Vasquez, E., Ogawa, T., Iturria-Medina, Y., Riera, J.J., Kawashima, R., 2011. An in vivo MRI template set for morphometry, tissue segmentation, and fMRI localization in rats. *Front. Neuroinformatics* 5, 26.
- Veraart, J., Leergaard, T.B., Antonsen, B.T., Van Hecke, W., Blockx, I., Jeurissen, B., Jiang, Y., Van der Linden, A., Johnson, G.A., Verhoye, M., Sijbers, J., 2011. Population-averaged diffusion tensor imaging atlas of the Sprague Dawley rat brain. *NeuroImage* 58, 975–983.
- Woelche, M., 1942. Eine neue Methode der Markscheidenfarbung. *J. Psychol. Neurol.* 199–202.
- Yushkevich, P.A., Piven, J., Hazlett, H.C., Smith, R.G., Ho, S., Gee, J.C., Gerig, G., 2006. User-guided 3D active contour segmentation of anatomical structures: significantly improved efficiency and reliability. *NeuroImage* 31, 1116–1128.